DOI: 10.1002/ejic.201100815

Crystal Growth and Structure of the New Ferrimagnetic Oxyphosphate $PbFe_3O(PO_4)_3$

Hassan El Hafid,[a] Matias Velázquez,*[a] Olivier Pérez,[b] Abdelaziz El Jazouli,[c] Alain Pautrat,[b] Rodolphe Decourt,[a] Philippe Veber,[a] Oudomsack Viraphong,[a] and Claude Delmas[a]

Keywords: Ferromagnetism / Magnetic properties / Phosphates / Phase transitions / Critical point phenomena

A new oxyphosphate, $PbFe_3O(PO_4)_3$, has been discovered and its structure has been characterized by single-crystal XRD between 293 and 973 K (monoclinic, space group $P2_1/m$, a = 7.5826 Å, b = 6.3759 Å, c = 10.4245 Å, β = 99.956°, Z = 2, at r.t.). Direct-current (DC) magnetic susceptibility and specific heat measurements performed on single crystals revealed an unusual sequence of second-order ferromagnetic-like phase transitions at T_{c1} = 31.8 K, T_{c2} = 23.4 K and $T_{c3} \approx$ 10 K. Alternating-current (AC) magnetic susceptibility measurements suggest glass-like dynamics between ca. 20 K and T_{c3}.

Introduction

Chemically-stable phosphate and oxyphosphate crystals have been widely investigated for nonlinear optics, magneto-optics and laser physics. The exceptionally high absorption cross-sections around 800 nm (ca. 10^{-18}–10^{-19} cm^2) and high 4f intraconfigurational optical transition oscillator strengths (ca. 10^{-5}–10^{-6}) of crystals of Nd-doped YPO_4 have been found to result from covalent interactions between the rare-earth 4f and 5d states and the mainly O 2p state valence band top levels.[1] The intense Eu^{3+} $^5D_0 \rightarrow {}^7F_0$ emission in $Ca_{10-x}Eu_x(PO_4)_6O_{1+x/2}$ has been interpreted in terms of J–J' mixing, which arises from both an unexpectedly high B_0^2 crystal field parameter (ca. –2000 cm^{-1}) and a low-lying $^7F_1$ energy level (deduced from low-temperature magnetic susceptibility measurements).[2] For pentaphosphates $Nd_xT_{1-x}P_5O_{14}$ (T = Y, La; $0.1 \leq x \leq 1$), the optical spectroscopy of the crystalline solid solutions has also been exhaustively investigated in the bulk crystal shape. Laser operation at 637.4 and 717 nm was demonstrated with PrP_5O_{14} crystals,[3–5] at 1051 nm with NdP_5O_{14} crystals[4,6] and at 1055 nm with $K_3Nd(PO_4)_2$ crystals.[7] Laser operation around 1048 nm was also established in a series of tetraphosphate $LiNd_{0.5}RE_{0.5}P_4O_{12}$ (RE = Gd, La) and $LiNdP_4O_{12}$ crystals, which exhibit large $\sigma_{em}\tau_R \approx 3.8 \times 10^{-23}$ cm^2 s parameters.[8] Efforts have been dedicated to the growth, spectroscopic and optical characterization of pure and RE^{3+}-doped (RE = Nd, Er) $KTiOPO_4$ and $RbTiOPO_4$ crystals and $RbTiOPO_4$ crystals that are co-doped with Yb^{3+} and Nb^{5+} ions for second-harmonic generation elements of Nd:YAG, optical parametric oscillator systems and self-frequency doubling generation.[9–11] The modification of the $^4F_{9/2}$ spin–orbit multiplet fluorescence of the Dy^{3+} cations in $DyPO_4$ crystals, which behave as 3D Ising antiferromagnets with T_N = 3.4 K, was studied as a function of electric-field polarization and magnetic field at low temperature.[12] Owing to their structural diversity, which allows us to explore the effect of low dimensionality on their magnetic properties, and the chemical disorder and different valencies that lead to distinct spin-sublattices, many transition metal phosphates have been studied: the Kosterlitz–Thouless transition of antiferromagnetic (T_N = 23.5 K) $BaNi_2(PO_4)_2$ crystals[13] and the spin–glass (SG)-like behaviour of β-$(NH_4)Fe_2(PO_4)_2$ crystals[14] are striking examples.

In this paper, we report the synthesis, crystal growth, crystal structure and static, macroscopic magnetic properties of a new lead iron oxyphosphate, $PbFe_3O(PO_4)_3$. Single crystals of this compound exhibit three ferromagnetic-like phase transitions at T_{c1} = 31.8 K, T_{c2} = 23.4 K and $T_{c3} \approx$ 10 K. Preliminary AC magnetic susceptibility measurements suggest the existence of some glass-like dynamics between ca. 20 K and T_{c3}.

[a] CNRS, Université de Bordeaux, ICMCB,
87 avenue du Dr. A. Schweitzer, 33608 Pessac cedex, France
[b] Laboratoire de Cristallographie et Sciences des Matériaux, UMR 6508 CNRS/Université de Caen,
6 Boulevard du Maréchal Juin, 14050 Caen cedex 04, France
[c] Laboratoire de Chimie des Matériaux Solides, URAC 17, Université Hassan II Mohammedia, Faculté des Sciences Ben M'Sik,
Casablanca, Morocco
Fax: +33-5-40-00-27-61
E-mail: matias.velazquez@icmcb-bordeaux.cnrs.fr
Supporting information for this article is available on the WWW under http://dx.doi.org/10.1002/ejic.201100815.

Results and Discussion

Crystal Structure and Crystal Faceting

The crystal structure of $PbFe_3O(PO_4)_3$ was solved with a $P2_1/m$ monoclinic cell between room temperature and 973 K with the lattice parameters that are indicated in Table 1. It was found to be isostructural with $AFe_3O(PO_4)_3$ (A = Ca,[15] Sr).[16] In the 3D structure, there are three crystallographically nonequivalent transition metal cation sites (Figure 1, a). Elongated [Fe(1)O_6] octahedra, of point group symmetry *i*, share two opposite edges to form an infinite chain along the *b* axis. The distorted [Fe(2)O_6] octahedra, which are somewhat compressed in the *b* direction, and the slightly distorted [Fe(3)O_5] square pyramids are connected through a vertex. The [Fe(2)O_6] octahedra also share a vertex with the [Fe(1)O_6] octahedra in such a way as to form a "millipede" with *b*/2-translated "legs". These millipedes are connected to each other by tetrahedral phosphate groups, which yields layers parallel to the *b* direction (Figure 1, a). These layers are linked to each other to form the 3D structure through three crystallographically nonequivalent phosphate tetrahedra (Figure 1, b). Figures 2 (a and b) show how these three phosphate tetrahedra connect the [Fe(1)O_6]-based chains. The [P(1)O_4] tetrahedra are bonded through an edge to the [Fe(2)O_6] octahedra and by two vertices with two successive [Fe(1)O_6] octahedra, which belong to a chain located in the nearest layer that contains the [Fe(2)O_6] octahedra, and the Fe(2)O_6, P(1)O_4 and Fe(1)O_6 linkage is approximately parallel to the [20–1] direction. The [P(2)O_4] tetrahedra share three of their vertices in a [Fe(1)O_6]-based chain with two successive [Fe(2)O_6] octahedra and a [Fe(1)O_6] octahedron, and their fourth vertex with [Fe(3)O_5] square pyramids belonging to a [Fe(1)O_6]-based chain in the neighbouring layer; the P(2)O_4 and Fe(3)O_5 linkage is parallel to the [00–1] direction. The [P(3)O_4] tetrahedra share two of their vertices with two successive [Fe(3)O_5] pyramids that belong to the same [Fe(1)O_6]-based chain, a third vertex is shared with a [Fe(3)O_5] pyramid that belongs to the nearest neighbour [Fe(1)O_6]-based chain within the same layer and the fourth vertex is linked to a [Fe(2)O_6] octahedron that belongs to a [Fe(1)O_6]-based chain located within the nearest layer. This truly 3D crystal structure defines monocapped trigonal prisms that are occupied by Pb^{2+} cations (see parts c in Figures 1 and 3). Setting aside the slightly larger O^{2-}–Pb^{2+} bond lengths in $PbFe_3O(PO_4)_3$, this polyhedron is virtually the same in $AFe_3O(PO_4)_3$ (A = Ca,[15] Sr).[16] The ratio of the sum of the ionic radii of A^{2+} and oxygen ions to the average A–O bond lengths is very close to 1 for the three compounds. Hence, in $PbFe_3O(PO_4)_3$ the Pb $6s^2$ states might be hybridized with 6p and 5d ones but, as the anionic packing of this structure is not compact, even including some of the cations in this packing, it is difficult to see whether a stereochemical activity of the Pb^{2+} cation lone pair takes place. In fact, the two uncapped "faces" [O(1)–O(1)–O(4)–O(4) and O(1)–O(1)–O(2)–O(2)] of the trigonal prism face the square base of the [Fe(3)O_5] pyramids, and open the way to two kinds of channels, which are shown in Figure 1 (c). It is tempting to think that lone pairs occupy the volume in the biggest channel, but the nearest face of the prism has a smaller surface than that close to the small channel, which is inconsistent with a repulsive interaction between the lone pair and the oxygen anions.

Table 1. Details of XRD data collection and structure refinements for $PbFe_3O(PO_4)_3$ at room temperature and at 973 K. Reliability factors are based on *F*.

	293 K	973 K
Crystal system	monoclinic	monoclinic
Lattice centering	primitive	primitive
a	7.5826(3) Å	7.6076(5) Å
b	6.3759(7) Å	6.4017(4) Å
c	10.4245(6) Å	10.4771(4) Å
β	99.956(5)°	99.662(5)°
Space group	$P2_1/m$	$P2_1/m$
Wavelength [Å]	0.71073	0.71073
Scan strategy	ϕ/ω	Φ
Scan angle [°]	0.8	0.8
Dx [mm]	34	40/60
$(\sin\theta/\lambda)_{max}$	0.94	0.8
	$-14 \le h \le 14$	$-12 \le h \le 12$
	$0 \le k \le 12$	$0 \le k \le 10$
	$0 \le l \le 19$	$0 \le l \le 12$
Measured reflections	10057	14046
Unique reflections	3644	1894
Unique reflections with $I \ge 3\sigma(I)$	3409	1599
Absorption correction	Gaussian integration based on the crystal morphology	SADABS [34]
$T_{min.}/T_{max.}$	0.099/0.446	–
Internal *R* value [%]		
before correction (obsd./all)	8.63/8.65	8.43/8.45
after correction (obsd./all)	4.63/4.65	3.06/3.19
Refinement program	JANA2006 [32]	JANA2006 [32]
Number of refinement parameters	113	113
Weighting method	Σ	Σ
$\rho_{min.}/\rho_{max.}$ [e/Å^3]	2.43/–4.56	2.41/–1.58
F(000)	618	618
Reliability factors (*R*/*Rw*)	0.032/0.044	0.025/0.029

All the single crystals obtained by the method described in the Exp. Section were strongly faceted with prominent (001) faces. According to classical theories,[17] which exclusively treat very slow growth rates, the growth kinetics of a given (*hkl*) face is considered to be driven by the decrease in free energy that its advancement permits. Consequently, the slowest-growing faces, which ultimately give rise to the crystal shape, correspond to those whose growth entails the smallest lowering of the free energy. As surface tensions are scarcely known for several (*hkl*) faces and are by definition unknown for a new crystal, it has become customary to use the d_{hkl} spacings of the crystal structure in order to guess a priori the faces that are likely to bind the crystal (the Bravais–Friedel–Donnay–Harker law). In $PbFe_3O(PO_4)_3$ at 973 K, the highest d_{hkl} spacings decrease in the series

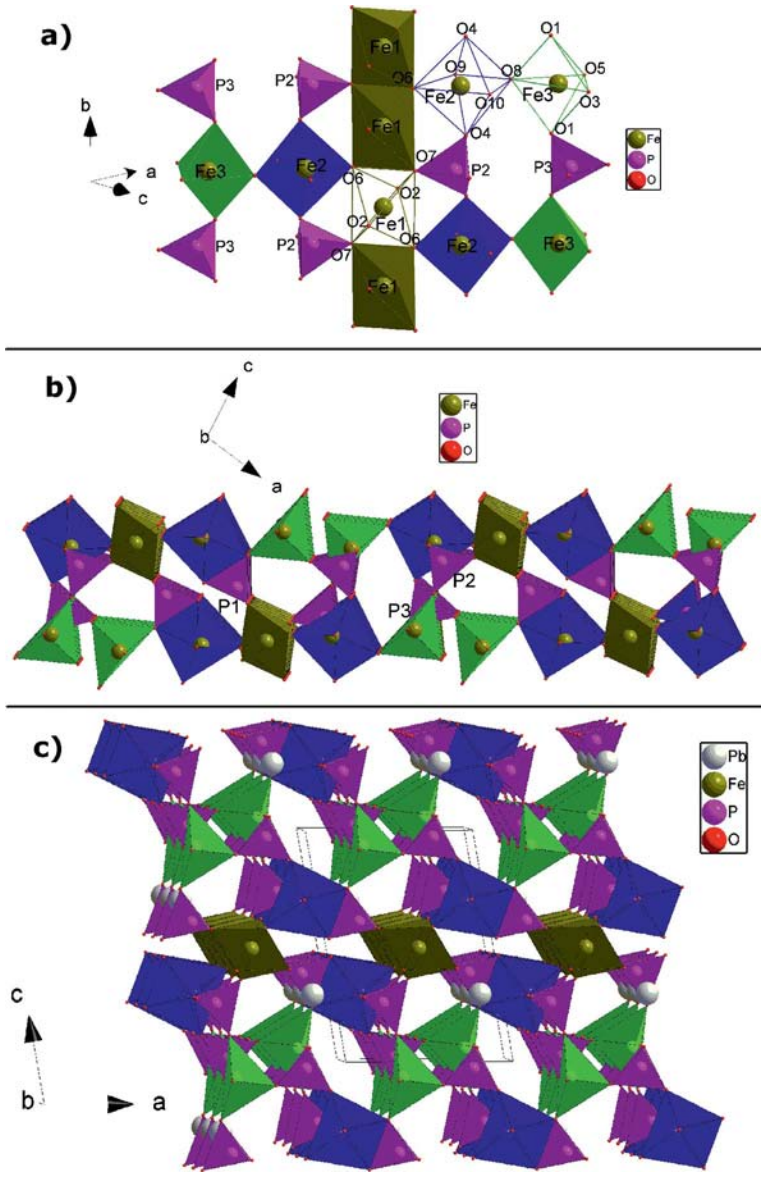

Figure 1. (a) Simplified view showing how the $Fe(1)O_6$, $Fe(2)O_6$ and $Fe(3)O_5$ octahedra are connected in the *b* direction to form a chain, together with the oxygen labels in each Fe^{3+} environment. Connections of these chains by the $P(2)O_4^{3-}$ and $P(3)O_4^{3-}$ tetrahedra lead to a layer parallel to the *b* direction. (b) Simplified view showing how the connections through $P(1)O_4^{3-}$, $P(2)O_4^{3-}$ and $P(3)O_4^{3-}$ tetrahedra, between the $Fe(2)O_6$- and $Fe(3)O_5$-legged $Fe(1)O_6$ chains lead to the general structure shown in (c). (c) Drawing of the whole $PbFe_3O(PO_4)_3$ crystal structure at room temperature ($P2_1/m$).

$d_{001} > d_{100} > d_{-101} > d_{010} > d_{101}$, with $d_{001} = c$ being substantially larger than $d_{100} = a$. From this perspective, the d_{hkl} spacings are empirically related to the lattice energy and, above all, to the strength and anisotropy of the chemical bonds within a given (*hkl*) plane. Careful analysis of the atomic d_{001}, d_{100}, d_{-101}, d_{010} and d_{101} layers, based on Coulombic interactions between purely ionic species and assuming that phosphate groups are not destroyed in the liquid phase, clearly shows that the density of chemical bonds decreases according to this series of planes, which is consistent with the faceting observed. The thermal expansion of lattice parameters between room temperature and 973 K is shown in parts a–c of Figure 4. The relative density change from 973 K to room temperature is rather small, ca. –1.4%. The mean lattice expansion coefficients $1/a(293\ K) \times da/dT \approx 5.7 \times 10^{-6}\ K^{-1}$, $1/b(293\ K)\, db/dT \approx 5.0 \times 10^{-6}\ K^{-1}$ and $1/c(293\ K) \times dc/dT \approx 7.6 \times 10^{-6}\ K^{-1}$, where *a*, *b* and *c* are the lattice parameters and *T* is temperature, are moderate in comparison with those of compounds such as KPb_2Cl_5,[18] in which anharmonic contributions to interatomic potentials are expected to be higher. The anisotropic increase in the thermal expansion of lattice parameters upon heating is consistent with the faceting observed and the smaller density of ionic bonds in the (001) plane than in the (100) and (010) ones. As they contain large channels (Figure 1, c) and are devoid of Pb, Fe(1) and Fe(2) cations, these planes have a particularly weak density of chemical bonds in comparison with the other faces.

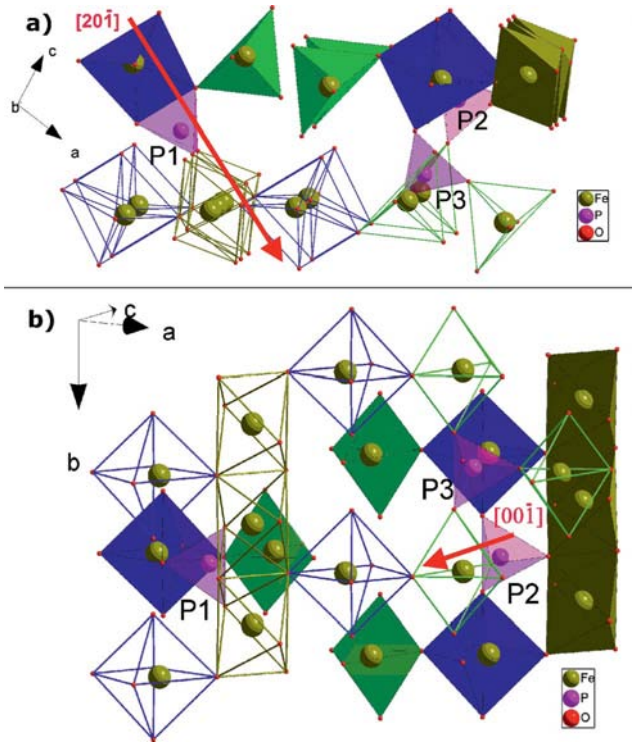

Figure 2. Details of the connections between the Fe(1)O_6-based chains by the three crystallographically nonequivalent [P(1)O_4^{3-}], [P(2)O_4^{3-}] and [P(3)O_4^{3-}] tetrahedra.

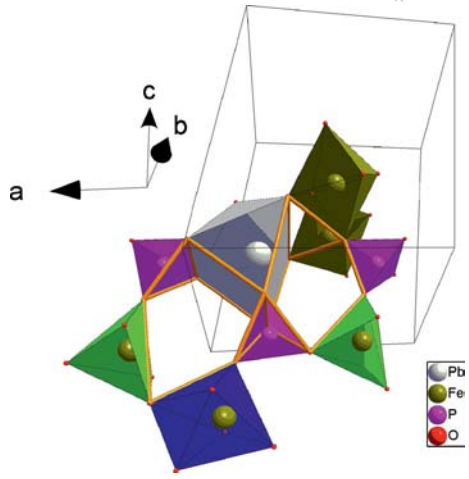

Figure 3. Simplified view showing how the uncapped faces of the PbO_7 distorted trigonal prism open onto the channels extending along the *b* direction.

Magnetic Properties

The low-field magnetic susceptibility displays a Curie–Weiss (C–W) behaviour from ca. 200–225 to 350 K, with a negative Curie paramagnetic temperature (θ_p) of –180.6 K, which indicates antiferromagnetic (AFM) interactions between the electronic spins, and a Curie constant (*C*) of

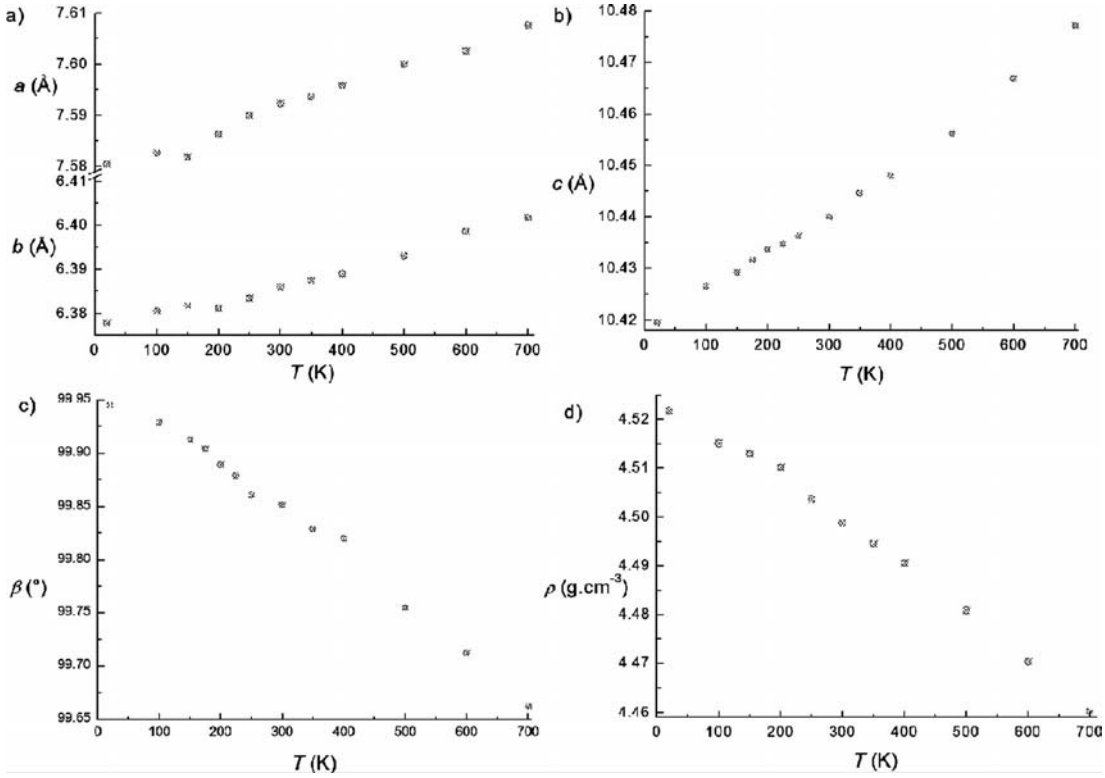

Figure 4. (a), (b), (c) Thermal dependence of the $PbFe_3O(PO_4)_3$ lattice parameters. (d) Thermal dependence of the $PbFe_3O(PO_4)_3$ calculated volumic mass.

1.11 K, which leads to an effective magnetic moment of 5.95 μ_B/Fe very close to the theoretical free ion value of 5.916 μ_B/Fe (Figure 5). Three consecutive ferromagnetic (FM)-like phase transitions without thermal hysteresis are observed at T_{c1} = 31.8 K, T_{c2} = 23.4 K and $T_{c3} \approx 10$ K (Figure 6). FM correlations appeared at below ca. 200 K, i.e. ca. 6.3·T_{c1} (see below), and became dominant below 80 K in single crystals, as deduced from the minimum in the χT vs. T curve (Figure 5). However, the resulting magnetic susceptibility does not seem to develop as in a strong ferromagnet; once corrected for the demagnetizing field effect, the χ/χ_{C-W} ratio is only 4.1 at 40 K. In comparison, the magnetic susceptibility of $PbFe_3O(PO_4)_3$ at 40 K is ca. 1540 times lower than that of the parallel susceptibility ($\chi_{\parallel}$) of $La_{1.2}Sr_{1.8}Mn_2O_7$ at its 2D–3D crossover temperature.[19] The $|\theta_p|/T_{c1}$ ratio of ca. 5.7 suggests that the AFM couplings are frustrated. The series of asymmetric "λ"-type specific heat discontinuities at low temperature confirmed the sequence of FM-like phase transitions at $T_1 \approx 31.2$ and $T_3 \approx 10.4$ K, and a slight rounded cusp at $T_2 \approx 24.9$ K (Figure 7). The absence of thermal hysteresis around the transition temperatures and the shape of the peaks lead us to conclude that these phase transitions are second order and typical of Heisenberg or Ising 3D magnetic systems. As FM correlations do not seem to grow very much, we evaluated the entropy associated with these specific heat peaks with a rough baseline, which amounts to $\Delta S_{1-2} \approx -0.15$ and $\Delta S_3 \approx -0.53$ R in the single crystal. The sum of these entropy changes corresponds to ca. 40% of the entropy change expected for a classical paramagnetic–FM transition of a S = 5/2 spin assembly. The separation observed between the zero-field-cooled (ZFC) and field-cooled (FC) magnetization curves suggests either a SG-like behaviour below the paramagnetic–FM transition temperature (T_{c1}), or a pinning of the magnetic domain walls (Figure 6). Below T_{c3}, as the temperature decreases, the magnetization of the single crystals decreases in the ZFC mode, whereas it increases in the FC mode. The absence of magnetization jumps or discontinuities in the low FC curves also confirms the second-order character of the phase transitions, and the Arrott plot of the isothermal magnetization in the vicinity of the first transition permits the unambiguous determination of T_{c1} = 31.8 K (Figure 8). The $|\theta_p|/T_{c1} \approx 5.7$ ratio, the simultaneous occurrence of FM and AFM interactions, the possibility of frustration together with the "mixture" of Fe^{3+} single ion anisotropies in this crystal structure (see below), the markedly different behaviour between the ZFC–FC magnetization curves and the slight magnetization drop below T_{c3} allow the presumption of an SG-like behaviour

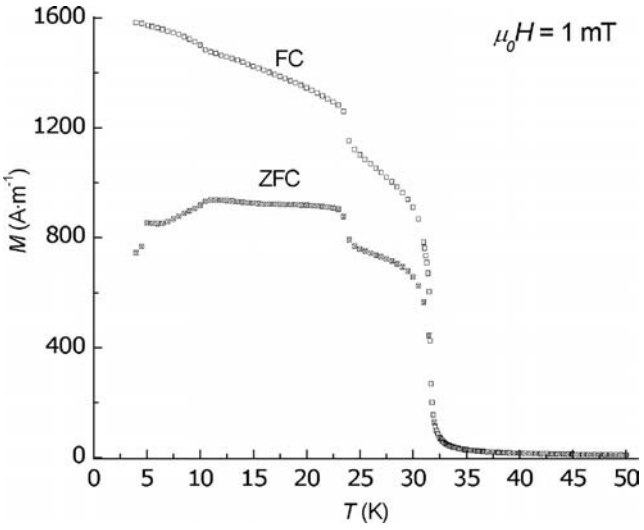

Figure 6. $PbFe_3O(PO_4)_3$ ZFC–FC spontaneous magnetization in low field measured from misoriented crystals.

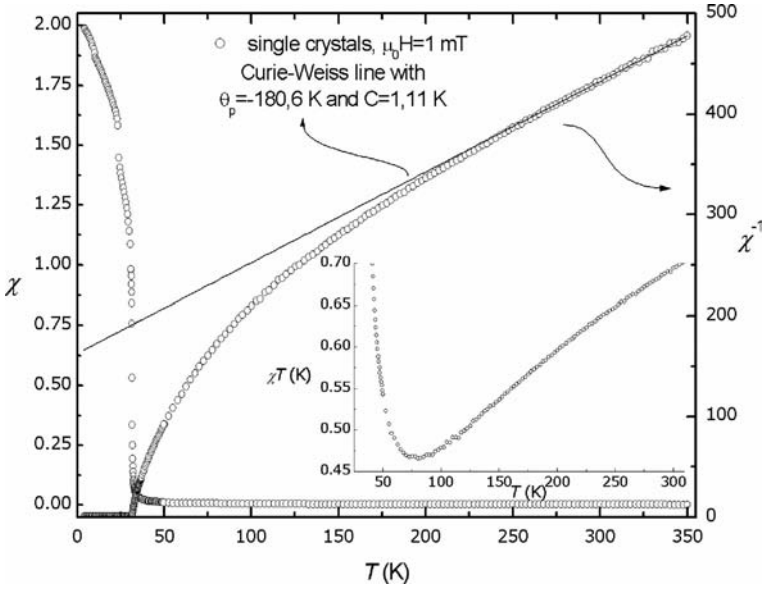

Figure 5. Temperature dependence of the $PbFe_3O(PO_4)_3$ magnetic susceptibility in low field measured with misoriented single crystals. Inset is shown the χT vs. T plot, which exhibits a minimum at ca. 80 K.

at temperatures below T_{c1} = 31.8 K. In $SrFe_3O(PO_4)_3$ powders, Belik et al. also identified an FM phase transition at T_c = 23.5 K and a re-entrant spin–glass freezing temperature of T_f = 22.4 K, by DC and AC magnetic susceptibility, ZFC–FC magnetization and specific heat measurements.[20] Isothermal magnetization measurements recorded after low-field cooling show the magnitude of the FM moments involved, as at T = 4.2 K and $\mu_0 H$ extrapolated at 0 T from the high field part of the curve, μ = 3.04 μ_B/Fe (Figure 9). This represents ca. 51% of the effective magnetic moment determined in the low field magnetic paramagnetic susceptibility. Note that the value of $M/M_{sat} \approx 0.52$ at 4.2 K and 4.8 T is independent of the magnitude of the field applied during cooling from 1 mT to 4.8 T. Figure 9 displays the isothermal magnetization cycle at 4.2 K, which was performed after an FC in 5 mT. The magnetic moments at 4.8 T are consistent with those in Figure 8, and no coercive field could be measured, which reveals either the presence of a very soft ferrimagnet or the vicinity of some compensation point as in the mixed SG–FM insulating compound Co_2TiO_4.[21] Figure 10 displays the real and imaginary parts

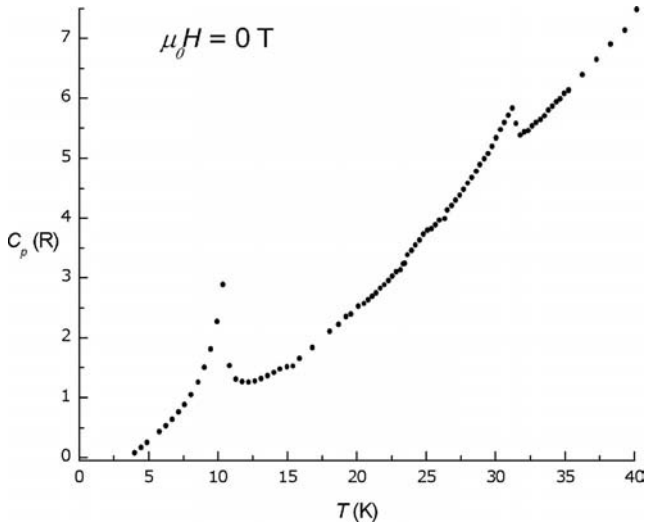

Figure 7. Temperature dependence below 40 K of the $PbFe_3O(PO_4)_3$ specific heat in zero field measured from a single crystal.

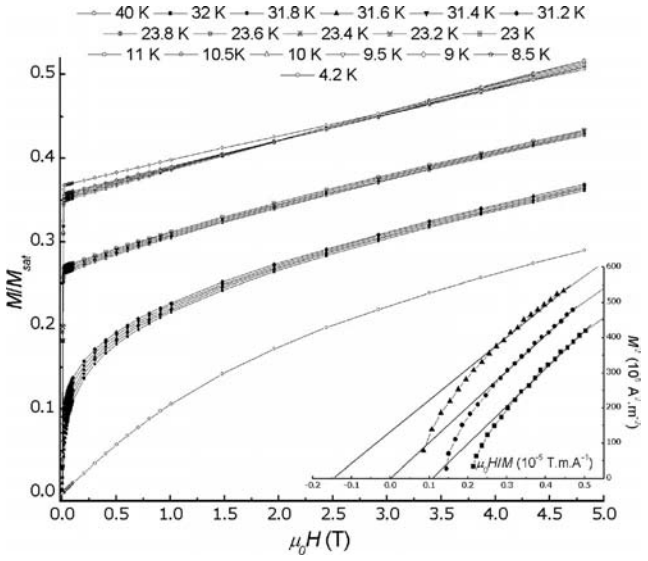

Figure 8. Isothermal magnetization in both FM and paramagnetic states for a $PbFe_3O(PO_4)_3$ crystal with $\mu_0 H$ parallel to (001) planes and M_{sat} = 186813.46 A m^{-1}. Inset is shown an Arrott plot that establishes T_{c1} = 31.8 K.

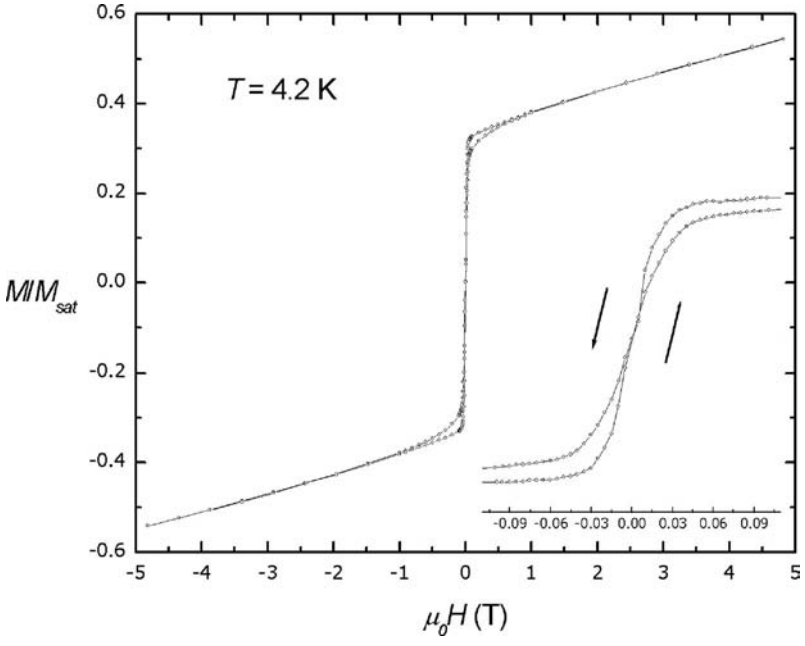

Figure 9. Magnetic cycle in the weakly FM state (T = 4.2 K). Ordinates represent M/M_{sat} where M_{sat} = 186813.46 A m^{-1}. The magnetization at 4.8 T is independent of the field applied upon cooling (0.001, 0.005 or 4.8 T).

of the magnetic susceptibility upon crossing the phase transitions sequence under B = 100 G with frequencies of 10^{-1} and 10^3 Hz. The imaginary part clearly evidences a strong dispersion for temperatures between T_{c1} and T_{c3}. Noticeably, two frequency-dependent peaks can be identified, which implies that several dissipative mechanisms are involved. The peak at higher temperature corresponds to an activated mechanism, the characteristic relaxation time of which follows an Arrhenius law $\tau = 2\pi/f = \tau_0 \cdot exp(\Delta/T)$, with $\tau_0 \approx 10^{-10}$ s and $\Delta \approx 240$ K. This indicates a classical magnetic domain wall propagation, which is consistent with long-range ferrimagnetic ordering at T_{c1}. The frequency spectra exhibit a profile slightly larger than that resulting from a Debye-type law, which suggests that the activation energy is well defined. The other peak, at lower temperature, corresponds to a substantial profile change of the spectra, which became logarithmic as expected for glassy dynamics.[22,23] Finally, for $T \leqslant T_{c3}$, the AC susceptibility decays abruptly and becomes virtually nil, which might be explained by the magnetic ordering evidenced by the specific heat peak at T_{c3}. The glass-like dynamic response between ca. 20 K and T_{c3} is very complex and its analysis is in progress.

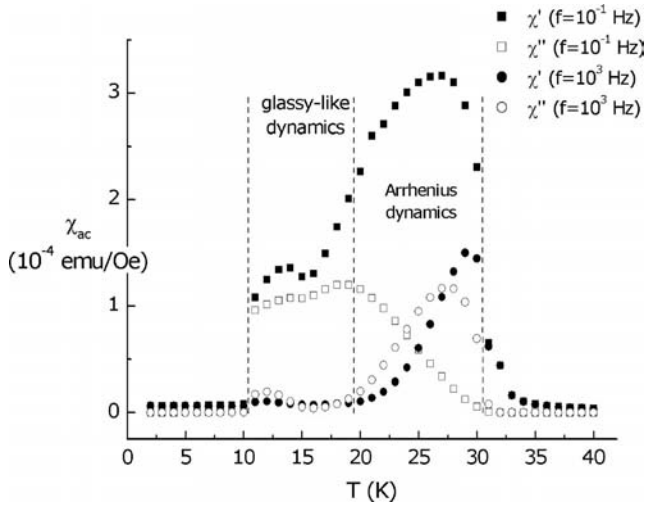

Figure 10. AC magnetic susceptibility measured from $PbFe_3O(PO_4)_3$ single crystals under a main field of 100 G and an AC field of 1 G with frequencies of 10^{-1} and 10^3 Hz.

Discussion

At least three different superexchange (SE) and thirteen supersuperexchange (SSE) pathways can be recognized in this crystal structure (Table 2, Figure 11). Most result in AFM couplings in such a way that the overall magnetic behaviour at low temperature is 3D. In the simplest cases, the sign and magnitude of these couplings can be roughly guessed by the Goodenough–Kanamori–Anderson (GKA) rules.[24] For example, these rules predict that a 180° Fe–O–Fe coupling yields strong AFM exchange integrals (ca. 750 K, strong σ AFM overlapping and weak π AFM overlap), 90° Fe–O–Fe coupling leads to moderate AFM exchange integrals (ca. 200 K, σ and π AFM overlap) and 180° Fe–O–O–Fe coupling results in weak AFM exchange integrals (ca. 75 K). The importance of SSE couplings in some transition metal phosphate compounds has been firmly established by DFT calculations.[25,26] The GKA rules also predict that for some Fe–O–Fe angles between 125 and 150° an upturn in the exchange sign should occur. Figure 11 illustrates very simply how frustration is likely to occur in $PbFe_3O(PO_4)_3$. On the one hand, the Fe(2) cations cannot be simultaneously FM coupled with Fe(1) and Fe(3) cations (J_1 and J_3) and AFM coupled with each other (J_4), and on the other hand, the Fe(3) cations cannot be simultaneously FM coupled with Fe(2) cations (J_3) and AFM coupled with each other (J_5). Powder XRD and electron probe microanalysis (EPMA) demonstrate that the pure and stoichiometric single crystals contain a very low level of chemical disorder and virtually no structural disorder, which is not incompatible with the appearance of spin–glass behaviour.[27] Mean-field theories exist that predict the likelihood of magnetic phase transitions sequence and mixed magnetic states for which the term "semi-spin–glass" was coined.[28] For instance, starting from a 3D Heisenberg Hamiltonian and a Gaussian distribution of magnetic couplings, Gabay and Toulouse predicted a T–J_0 magnetic phase diagram in zero field, in which FM and SG behaviour coexists.[29] Although J_0 is directly related to the Fe content and the distribution of magnetic exchange couplings are directly related to the chemical disorder, there is a clear discrepancy between our measurements and the third order character of the M1–M2 transition that they predicted, which can hardly be observed by means of temperature-dependent susceptibility measurements, but requires specific heat (C_p) data recorded with a very stable temperature regulation to be identified through the $\partial(C_p/T)/\partial T$ discontinuity. In addition, in the temperature range that we investigated, the magnetization does not vanish.

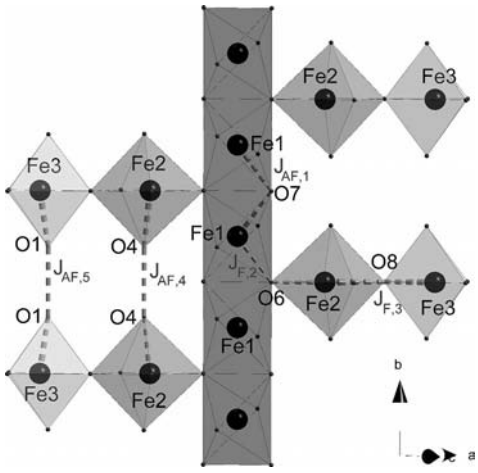

Figure 11. An attempt to illustrate how magnetic frustration may occur in $PbFe_3O(PO_4)_3$ based on tentative assignment of the five most obvious SE and SSE couplings.

Table 2. Possible SE and SSE pathways through neighbouring oxygen atoms in $PbFe_3O(PO_4)_3$ based on structural parameters.

Label and exchange sign	Exchange path	Successive bond angle [°]	Torsion angle [°]	Successive bond lengths [Å]
$J_1 < 0$	Fe1–O6–Fe1	Fe1–O6–Fe1 106.16 Fe1–O7–Fe1 96.79	–	O6–Fe1 1.993 Fe1–O7 2.132
$J_2 > 0$	Fe2–O6–Fe1	Fe2–O6–Fe1 125.49	–	Fe2–O6 1.871 O6–Fe1 1.993
$J_3 > 0$	Fe3–O8–Fe2	Fe3–O8–Fe2 125.62	–	Fe3–O8 2.000 O8–Fe2 2.310
$J_4 < 0$	Fe2–O4–O4–Fe2	Fe2–O4–O4 174.02 O4–O4–Fe2 174.02	0	Fe2–O4 1.991 O4–O4 2.416 O4–Fe2 1.991
$J_5 < 0$	Fe3–O1–O1–Fe3	Fe3–O1–O1 171.23 O1–O1–Fe3 171.23	0	Fe3–O1 1.983 O1–O1 2.456 O1–Fe3 1.983
J_6	Fe3–O5–O1–Fe3	Fe3–O5–O1 115.54 O5–O1–Fe3 110.98	70.63	Fe3–O5 1.878 O5–O1 2.537 O1–Fe3 1.983
J_7^{i}	Fe3–O1–O5–Fe3	Fe3–O1–O5 110.98 O1–O5–Fe3 115.54	70.63	Fe3–O1 1.983 O1–O5 2.537 O5–Fe3 1.878
J_8	Fe2–O10–O5–Fe3	Fe2–O10–O5 105.76 O10–O5–Fe3 174.49	180.00	Fe2–O10 1.938 O10–O5 2.511 O5–Fe3 1.878
J_9	Fe2–O4–O3–Fe3	Fe2–O4–O3 118.63 O4–O3–Fe3 136.36	62.59	Fe2–O4 1.991 O4–O3 2.558 O3–Fe3 1.928
J_{10}[a]	Fe3–O3–O4–Fe2	Fe3–O3–O4 136.36 O3–O4–Fe2 118.63	62.59	Fe3–O3 1.928 O3–O4 2.558 O4–Fe2 1.991
J_{11}[a]	Fe3–O5–O10–Fe2	Fe3–O5–O10 174.49 O5–O10–Fe2 105.76	180.00	Fe3–O5 1.878 O5–O10 2.511 O10-Fe2 1.938
J_{12}	Fe3–O3–O7–Fe1	Fe3–O3–O7 159.89 O3–O7–Fe1 131.55	87.65	Fe3–O3 1.928 O3–O7 2.511 O7–Fe1 2.132
J_{13}[b]	Fe3–O8–O2–Fe1	Fe3–O8–O2 118.33 O8–O2–Fe1 148.81	52.00	Fe3–O8 2.000 O8–O2 2.534 O2–Fe1 1.997
J_{14}[c]	Fe2–O9–O4–Fe2	Fe2–O9–O4 155.84 O9–O4–Fe2 109.84	32.65	Fe2–O9 2.104 O9–O4 2.917 O4–Fe2 1.991
J_{15}[b]	Fe2–O8–O2–Fe1	Fe2–O8–O2 108.40 O8–O2–Fe1 148.81	156.77	Fe2–O8 2.310 O8–O2 2.534 O2–Fe1 1.997
J_{16}[b]	Fe2–O9–O2–Fe1	Fe2–O9–O2 114.72 O9–O2–Fe1 138.52	175.07	Fe2–O9 2.104 O9–O2 2.556 O2–Fe1 1.997

[a] $J_7 = J_6$, $J_{10} = J_9$, $J_{11} = J_8$. [b] This coupling occurs twice. [c] Presence of Pb cation in the exchange pathway.

Conclusions

We have synthesized and grown single crystals of the new oxyphosphate $PbFe_3O(PO_4)_3$, the magnetic behaviour of which may open a possibility to test spin–glass/FM or AFM coexistence theories with real systems of localized 5/2 spins in a virtually nondisordered phase. The closeness of the three FM-like magnetic phase transitions observed for the first time, thanks to single-crystalline samples, may offer an opportunity to investigate the vicinity of multicritical points in T–J_0 phase diagrams in a fixed $\mu_0 H$ field. In single crystals, partially substituting Pb^{2+} cations for another divalent cation and/or substituting the Fe^{3+} cations for nonmagnetic ones should help to control the crystallochemical disorder in order to understand and rationalize its peculiar ferrimagnetic behaviour. AC magnetic susceptibility measurements reveal glass-like dynamics in some ferrimagnetic state, the analysis of which (together with remanent magnetization relaxation measurements) is in progress and will constitute a separate publication. The exact nature of the successive magnetic phases at low temperature will be firmly established by elastic and inelastic neutron diffusion. The critical behaviour (universality class, possible crossovers) must also be characterized from well-oriented single crystals with an optimized demagnetizing field factor.

Experimental Section

Synthesis, Powder XRD and Crystal Growth: Crystals of $PbFe_3O(PO_4)_3$ were grown by a combination of self-flux and vertical Bridgman methods.[30] One advantage of combining high-temperature solution growth with a directional solidification method such as vertical Bridgman's is the separation of bulk portions grown successively, which adopt a different phase content and associated microstructure at each equilibrium phase relationship change. The powder phase was prepared by coprecipitation from $Pb(NO_3)_2$, $Fe(NO_3)_3{\cdot}9H_2O$ and $(NH_4)_2HPO_4$ (1:3:3), first dissolved separately in a minimum volume of distilled water, then mixed, dried at 100 °C and thermally treated at 200 and 400 °C to remove ammoniac, residual water and nitrate groups. The resulting powder was carefully ground and placed in a sealed rubber tube to undergo hydrostatic compression into rods at pressures up to 1500 $kg\,cm^{-2}$. The rods were sintered at 880 °C for 72 h. Powder XRD confirmed the formation of the $PbFe_3O(PO_4)_3$ phase together with a minor unknown phase. The $PbFe_2(P_2O_7)_2$ "solvent" powder was prepared by the same process. A powder mixture (40 g) of molar ratio $PbFe_2(P_2O_7)_2/PbFe_3O(PO_4)_3$ = 1:5 was sealed in air inside a vertical platinum crucible, which was transferred to a vertical Bridgman furnace equipped with two independent heating zones. The crucible was kept at a soaking temperature of 950 °C for 60 h before the temperature of the upper zone was set at 890 °C and that of the lower zone at 835 °C with a typical thermal gradient, previously measured inside the empty furnace, in the adiabatic zone of ca. 16 $°C\,cm^{-1}$. The crucible translation rate was fixed at 0.25 $mm\,h^{-1}$. Once the crucible had been translated in the lower zone, the upper zone temperature was equilibrated with that of the lower zone and a cooling rate of 12 $°C\,h^{-1}$ was applied. Deep red, plate-like single crystals were extracted from the growth load.

Powder XRD, Scanning Electron Microscopy (SEM) and Elemental Analysis: Several pieces of the growth load were taken from various parts (the beginning, middle and solidification ends) and characterized by powder XRD in conjunction with SEM and energy-dispersive X-ray (EDX) spectroscopic elemental analysis. Le Bail fits of the XRD patterns revealed the presence of three phases in the first stages of growth: $PbFe_3O(PO_4)_3$, $Pb_3Fe_2(PO_4)_4$ and Fe_3PO_7. As growth proceeds, $Pb_3Fe_2(PO_4)_4$ vanishes and is progressively replaced by $FePO_4$. In spite of this multiphase formation, it is useful to employ $PbFe_2(P_2O_7)_2$ as the solvent because it lowers both the soaking and initial upper zone temperatures. Several cross-sections of sintered $PbFe_3O(PO_4)_3$ rods and many faceted single crystals were analyzed by SEM coupled with EDX. Although crystal facets were simply cleaned, slabs from $PbFe_3O(PO_4)_3$ sintered rods were cut with a wire saw. Analysis was performed with a JEOL 840 SE microscope with a tension of 15 kV. The compositional analysis showed that only crystal facets display the expected $PbFe_3O(PO_4)_3$ cationic stoichiometry. As elemental analysis was difficult to perform on the sintered rods slabs, mainly because of the random and nonuniform tilting of the grains, we decided to switch to EPMA.

EPMA Analysis: The chemical compositions were analyzed by EPMA with a CAMECA SX-100 apparatus working at 20 kV and 20 nA with a wavelength dispersive spectrometer. The quantitative determination was performed on the basis of intensity measurements of the L_α and M_α X-ray emission lines of Pb, and K_α X-ray emission lines of Fe and P, using metallic lead, metallic iron and an apatite as reference compounds. The oxygen content was deduced from the cationic composition to insure the charge balance. Thus the oxidation states of the lead, iron and phosphorus cations were assumed to be 3+, 2+ and 5+, respectively. For polycrystalline samples, $50 \times 50\ \mu m^2$ mapping of the elemental content was performed at various locations, whereas for single crystals, $150 \times 150\ \mu m^2$ mapping was performed on the (001) facetted surfaces. The typical penetration lengths of our experimental conditions were ca. 1.9 μm. Atomic content relative error for each measurement was estimated to be ca. 2.5%. As the single-crystal surface composition was particularly uniform and its cationic composition very close to the nominal one (Pb 4.7 ± 0.3 at.-%, Fe 15.8 ± 0.4 at.-% and P 14.6 ± 0.4 at.-%) we used it as a reference for comparisons with the elemental compositions obtained from polycrystalline pellets. In the EPMA data of the latter, we systematically eliminated the bad counting statistics that corresponded, in fact, to the porosities distributed over the whole surfaces investigated. By doing so, we could identify minority secondary phases, which are not necessarily the same as those found by powder XRD, and essentially found one dominant kind of cationic nonstoichiometry in the majority phase, namely Pb 5.0–6.2 at.-%, Fe 13.0–14.6 at.-% and P 15.1–16.1 at.-%.

Specific Heat, Magnetization and Magnetic Susceptibility Measurements: A single crystal (4.15 mg) was fixed to a sapphire sample holder with vacuum grease. The sample holder was mounted on the measurement shaft of a Quantum Design PPMS instrument interfaced to operate with a 2–τ pulse–step method corrected for the grease baseline. Magnetic susceptibility and ZFC–FC magnetization cycles were measured with a Quantum Design SQUID MPMS XL magnetometer, at the ICMCB, operating in the 4.2–350 K temperature range and in the 0–5 T magnetic field range. The single crystals, with masses ranging from 4.15 to 22.3 mg, were mounted in a capsule placed in a straw and the negligibly small diamagnetic contribution of the capsule was not subtracted from our data. As the single crystals were misoriented with respect to each other and their demagnetizing field factor was not optimized (ca. 6.5–10 in the growth plane), we could not extract reliable critical exponents from our data, even if they do fit correctly to some power law. The dimensionless MKSA susceptibility was calculated with the room-temperature volumic mass of 4.52 $g\,cm^{-3}$, which was determined by single-crystal XRD. AC magnetic susceptibility measurements were also performed with a Quantum Design MPMS instrument, at the CRISMAT laboratory, under a main field of 100 G and an AC field of 1 G with a frequency ranging from 10^{-1} to 10^3 Hz. It is clear that growing single crystals with optimized demagnetizing field factors in several crystallographic directions of interest stands as an important challenge to be taken up by crystal growers seeking to deepen our insight on the magnetic behaviour of this oxyphosphate.

Crystal Orientation by the Laue Method, Data Collection and Structure Determination: The orientation of the crystal facet was determined by the backscattered Laue method with a polychromatic Cu X-ray tube working at 40 kV and 40 mA. The crystal-screen distance was set at 6 cm. The preliminary XRD investigation was performed at room temperature with Mo-K_α radiation with a Kappa CCD (Bruker Nonius) diffractometer. Large ω and χ scans were used to control the crystalline quality of different samples and to determine cell parameters. A single crystal of suitable size ($150 \times 80 \times 35\ \mu m^3$) was selected. Owing to the cell parameters and the small spot size, a suitable data collection strategy was defined. A scanning angle of 0.8° and a *Dx* (detector–sample distance) value of 34 mm were chosen; ϕ and ω scans were used. To collect a great number of weak reflections, but avoid detector saturation by reflections of strong intensity, two different exposure times (64 s/° and 6 s/°) were used to collect data. The diffracted intensities were collected up to θ = 42°. Sections of the reciprocal space calculated from these series of experimental frames were sufficiently accurate

to obtain an overall view of the reciprocal space. The diffraction pattern can be described within a monoclinic cell [a = 7.5826(3) Å, b = 6.3759(7) Å, c = 10.4245(6) Å, β = 99.956(5)°]. The observed condition limiting the possible reflections, *0k0: l = 2n* is consistent with the space group $P2_1/m$. The EvalCCD software[31] was used to extract reflections from the collected frames. The reflections were merged and rescaled as a function of the exposure time. 3409 independent reflections with $I \geq 3\sigma(I)$ were obtained. An absorption correction based on a Gaussian integration method using the crystal morphology was applied with Jana2006.[32] Details of the data collection are reported in Table 1. A structural model considering the $P2_1/m$ space group was constructed with SUPERFLIP[33] using the charge flipping method. Lead, iron and phosphorus atoms were located. This first model leads to a reliability factor of ca. 17%, which was introduced in the refinement program Jana2006.[32] All the atomic positions were refined, and anisotropic displacement parameters were considered for all the atoms. This refinement led to an agreement factor of 14%. Fourier differences were then calculated, which allowed the location of ten oxygen atoms. The final refinement procedure leads to $R(obs)$ = 0.032 and $w_R(obs)$ = 0.044. Atomic parameters are summarized in Tables S1 and S3 and interatomic distances are listed in Table S2. The evolution of the cell parameters vs. temperature (room temperature–800 K) was performed on the same Kappa CCD (Bruker Nonius) diffractometer but now equipped with a Cyberstar gas blower system. The measurements at high temperatures required specific crystal packaging: the crystal was introduced into a quartz capillary and blocked with thin stems of quartz. To decrease the obstruction near the sample due to the conditioning apparatus and to avoid collisions or a direct contact of the gas flow with the detector, the *Dx* value was fixed at 60 mm and a classical procedure for determining cell parameters (large ω and χ scans) was applied for each temperature. The evolution of the cell parameters is summarized in Figure 4. Further details on the crystal structure investigation(s) may be obtained from the Fachinformationszentrum Karlsruhe, 76344 Eggenstein-Leopoldshafen, Germany (Fax: +49-7247-808-666; E-mail: crysdata@fiz-karlsruhe.de), on quoting the depository numbers CSD-423338 (at 293 K) and CSD-423337 (at 973 K).

Supporting Information (see footnote on the first page of this article): Atomic parameters and interatomic distances from the crystal structure determination.

Acknowledgments

The authors would like to thank the Aquitaine Region and the Groupement d'Intérêt Scientifique (GIS), Advanced Materials in Aquitaine for supporting this work and funding the PhD fellowship of H. E. H. and the French Centre National de la Recherche Scientifique (CNRS) and the Moroccan Centre National de la Recherche Scientifique et Technique for supporting the cooperation agreement no. 24494. Michel Lahaye is acknowledged for the EPMA characterization of the samples.

[1] O. Guillot-Noel, B. Bellamy, B. Viana, D. Gourier, *Phys. Rev. B* **1990**, *60*, 1668–1677.
[2] B. Piriou, D. Fahmi, J. Dexpert-Ghys, A. Taitai, J. L. Lacout, *J. Lumin.* **1987**, *39*, 97–103.
[3] B. Borkowski, E. Grzesiak, F. Kaczmarek, Z. Kaluski, J. Karolczak, M. Szymanski, *J. Cryst. Growth* **1978**, *44*, 320–324.
[4] M. Szymanski, J. Karolczak, F. Kaczmarek, *Appl. Phys.* **1979**, *19*, 345–351.
[5] M. Szymanski, *Appl. Phys.* **1981**, *24*, 13–20.
[6] R. D. Plättner, W. W. Krühler, W. K. Zwicker, T. Kovats, S. R. Chinn, *J. Cryst. Growth* **1980**, *49*, 274–290.
[7] S. R. Chinn, H. Y.-P. Hong, *Opt. Commun.* **1976**, *18*, 87–88.
[8] K. Otsuka, J. Nakano, T. Yamada, *J. Appl. Phys.* **1975**, *46*, 5297–5299.
[9] B. Boulanger, J. Zyss, *International Tables for Crystallography*, vol. D, *Physical properties of crystals*, chapter 7, *Nonlinear optical properties* (Ed.: A. Authier), Kluwer Acad. Publ., Dordrecht Boston, London, **2003**, p. 178–216.
[10] C. Zaldo, M. Rico, F. Díaz, J. J. Carvajal, *Optical Mater.* **1999**, *13*, 175–180.
[11] X. Mateos, V. Petrov, A. Peña, J. J. Carvajal, M. Aguilo, F. Diaz, P. Segonds, B. Boulanger, *Opt. Lett.* **2007**, *32*, 1929–1931.
[12] R. H. Petit, J. Ferré, J. Duran, *Phys. Rev. B* **1981**, *23*, 1216–1224.
[13] L.-P. Regnault, J. Rossat-Mignod, J. Y. Henry, L. J. De Jongh, *J. Magn. Magn. Mater.* **1983**, *31–34*, 1205–1206.
[14] L. Adam, A. Pautrat, O. Perez, P. Boullay, *Phys. Rev. B* **2010**, *82*, 054401.
[15] M. Hidouri, M. Ben Amara, *Acta Crystallogr., Sect. E* **2009**, *65*, i66.
[16] V. A. Morozov, K. V. Pokholok, B. I. Lazoryak, A. P. Malakho, A. Lachgar, O. I. Lebedev, G. van Tendeloo, *J. Solid State Chem.* **2003**, *170*, 411–417.
[17] E. Dowty, *Amer. Miner.* **1980**, *65*, 465–471.
[18] M. Velazquez, A. Ferrier, O. Perez, P. Gravereau, J.-P. Chaminade, R. Moncorgé, *Eur. J. Inorg. Chem.* **2006**, *20*, 4168–4178.
[19] M. Velázquez, J.-M. Bassat, J.-P. Renard, C. Dupas, A. Revcolevschi, *J. Phys. Condens. Matter* **2002**, *14*, 6667–6674.
[20] A. A. Belik, N. Tsujii, Q. Huang, E. Takayama-Muromachi, M. Takano, *J. Phys. Condens. Matter* **2007**, *19*, 145221.
[21] J. Hubsch, G. Gavoille, *Phys. Rev. B* **1982**, *26*, 3815–3823.
[22] T. Nattermann, Y. Shapir, I. Vilfan, *Phys. Rev. B* **1990**, *42*, 8577–8585.
[23] M. Giot, A. Pautrat, G. André, D. Saurel, M. Hervieu, J. Rodriguez-Carvajal, *Phys. Rev. B* **2008**, *77*, 134445, 1–7.
[24] J. B. Goodenough, *Magnetism and the Chemical Bond*, Wiley Interscience, New York, **1963**.
[25] H.-J. Koo, D. Dai, M.-H. Whangbo, *Inorg. Chem.* **2005**, *44*, 4359–4365.
[26] M.-H. Whangbo, H.-J. Koo, D. Dai, *J. Solid State Chem.* **2003**, *176*, 417–481.
[27] F. Ladieu, F. Bert, V. Dupuis, E. Vincent, J. Hammann, *J. Phys. Condens. Matter* **2004**, *16*, S735–S741.
[28] J. Villain, *Z. Physik B* **1979**, *33*, 31–42.
[29] M. Gabay, G. Toulouse, *Phys. Rev. Lett.* **1981**, *47*, 201–204.
[30] M. Velázquez, A. Ferrier, S. Pechev, P. Gravereau, J.-P. Chaminade, X. Portier, R. Moncorgé, *J. Cryst. Growth* **2008**, *310*, 5458–5463.
[31] A. Duisenberg, L. Kroon-Batenburg, A. Schreurs, *J. Appl. Crystallogr.* **2003**, *36*, 220–229.
[32] V. Petrıcek, M. Dusek, L. Palatinus, *JANA2006*, Institute of Physics, Praha, Czech Republic, **2006**.
[33] L. Palatinus, G. Chapuis, *J. Appl. Crystallogr.* **2007**, *40*, 786–790.
[34] G. M. Sheldrick, *Sadabs Program for Scaling and Correction of Area Detector Data*, Bruker AXS Inc., Madison, Wisconsin, USA, **2002**.

Received: August 1, 2011
Published Online: November 10, 2011

